A Self-Reconfigurable Variable-Stiffness Soft Robot Based on Boundary-Constrained Modular Units

Mohammad Amin Karimi, Vahid Alizadehyazdi, Heinrich M. Jaeger, and Matthew Spenko, *Senior Member, IEEE*

***Abstract*—This article describes a soft robot based on boundary constrained modular subunits. The loop-shaped robot consists of a granule-filled elastic toroidal membrane with a series of modular subunit robots attached to its exterior. The robot can operate both as a soft robot to conform to external objects or navigate through narrow corridors and as a rigid robot by jamming its internal granules using a vacuum. The jammed state is useful for exerting forces on the environment in object manipulation or locomotion tasks. This article describes the robot's design, object handling capabilities, locomotion, shape formation, and ability to navigate narrow corridors. We also present computationally efficient control methodologies used for self-reconfiguration and target tracking, which enable scaling the number of subunits to create larger systems. The robot's scalability and the control methodologies are verified through simulation with ProjectChrono, a multibody dynamic simulation platform. All other results are obtained experimentally.**

***Index Terms*—Boundary-constrained swarm, granular jamming, scalability, self-reconfiguration.**

I. Introduction and Background

SOFT robots can offer many advantages over traditional rigid robots, including conformability to different object geometries, shape changing, safer physical interaction with humans, the ability to handle delicate objects, and grasping without the need for high-precision control algorithms. As such, they have been utilized in many robotic applications, including arms and grippers [1]–[3], prosthetic devices [4], and fish-like robots [5]. Despite these advantages, soft robots often lack high force capacity, scalability, responsive locomotion and object handling, and a self-contained untethered design, all of which have hindered their adoption. To address these issues, this article describes a robot comprised of several rigid robotic subunits flexibly connected to their neighbors by a closed-loop, granule-filled, soft membrane that can jam the particles with an untethered vacuum [see Fig. 1(a)]. The robot was not designed for a given application; instead, it serves as a general platform to demonstrate this new concept. The jamming feature allows the robot to exert relatively large forces on objects in the environment. The modular design resolves the scalability issue. Using decentralized robotic subunits allows the robot to configure itself in a variety of shapes and conform to objects, all while locomoting. The result is a compliant high-degree-of-freedom (DOF) system with excellent morphability.

Force capacity: To manipulate objects and exert relatively large external forces, the robot can jam to modulate its stiffness [6]. Jamming structures in robotics can be generally categorized into fiber [7], layer [8], or granular jamming [2], [9]. Moreover, combinations of these can increase stiffness variation for compression, tension, bending, torsion, or shear loads [10]. The robot presented here uses granular jamming, similar to the universal gripper [2], for its isotropic stiffness variation properties and versatility in loading modes, i.e., compression, bending, and shear loading [7], [11].

Scalability: Most elastomeric soft robots are fabricated using soft 3-D printing, shape deposition manufacturing, or soft lithography [12], [13]. When scaling these designs up, fabrication becomes difficult and robustness may be reduced because of manufacturing defects. Also, repairing or reconfiguring the robot may prove challenging [14].

To overcome these issues, we have taken inspiration from modular self-reconfigurable robots, which typically have good scalabilty and robustness [15], [16]. However, other than a few systems made with soft parts [14], [17], [18], these robots do not exhibit the desired "soft" characteristics because they have rigid (or no) physical connections [19], [20]. The key difference in the robot described here is that the subunits do not need to be soft; rather, the compliant connection between them enables the collective to behave like a soft system.

Locomotion: The robot utilizes whegs (wheel-legs) [21] for locomotion, which enables a high traction force, rudimentary obstacle climbing, and a reasonable locomotion speed. Wheeled locomotion of soft robots was introduced in earlier versions of our work, where the initial design concept of a boundary-constrained modular soft robot was presented [22], [23].

Tethering: Due to the challenges of packaging hardware in soft robots, creating an untethered design is still an active issue [24], [25]. The modular design presented here distributes

Manuscript received February 8, 2021; revised July 8, 2021; accepted August 9, 2021. Date of publication September 20, 2021; date of current version April 5, 2022. This paper was recommended for publication by Associate Editor R. Kramer-Bottiglio and Editor M. Yim upon evaluation of the reviewers' comments. This work was supported by the National Science Foundation through the Emerging Frontiers in Research and Innovation Project under Grant 1830939. *(Corresponding author: Mohammad Amin Karimi.)*

Mohammad Amin Karimi and Matthew Spenko are with the Department of Mechanical, Materials, and Aerospace Engineering, Illinois Institute of Technology, Chicago, IL 60616 USA (e-mail: mkarimi1@hawk.iit.edu; mspenko@iit.edu).

Vahid Alizadehyazdi and Heinrich M. Jaeger are with the James Franck Institute, The University of Chicago, Chicago, IL 60637 USA (e-mail: vahid@uchicago.edu; h-jaeger@uchicago.edu).

This article has supplementary material provided by the authors and color versions of one or more figures available at https://doi.org/10.1109/TRO.2021.3106830.

Digital Object Identifier 10.1109/TRO.2021.3106830

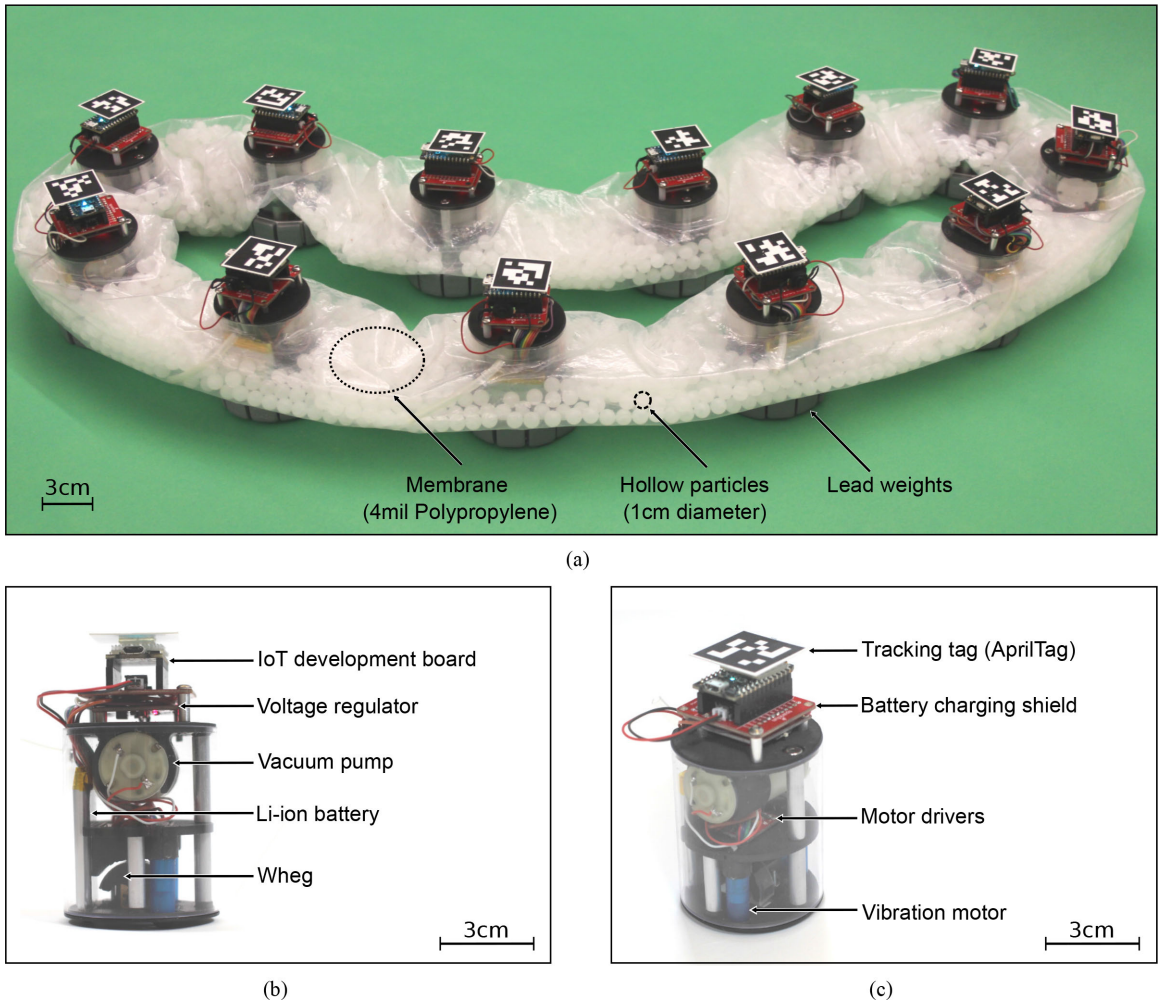

Fig. 1. (a) Robot is comprised of modular subunits connected to each other with a particle-filled compliant membrane. (b) Side view of the locomotion subunit. (c) Isometric view.

the hardware to achieve a self-contained design. Additionally, since the individual subunits do not need to be soft themselves, the system can utilize traditional rigid actuators and electronics. This is a major advantage since, despite the rapid evolution of flexible electronics and soft actuators [12], they still face limitations such as low responsiveness in shape memory alloys [26], low force capacity in dielectric elastomer actuation [27], or large equipment in fluidic elastomer actuation [28].

This article builds upon our prior work that presented the initial concept of a boundary-constrained modular soft robot [22]. This article presents a new robot design, highlights a new and more detailed control methodology, further demonstrates the robot's ability to grasp and exert loads on objects, and introduces the ability to navigate corridors and perform robustly when subunits fail. We also use a dynamic simulation to study scalability and control strategies. Section II describes the robot's design and fabrication. Section III details the control methodology. A dynamic simulation is presented in Section IV, and experimental results are covered in Section V.

II. Materials and Methods

This section details the robot's design and fabrication as well as the experimental test setup.

The robot consists of 12 identical subunit robots, evenly distributed 18 cm apart along a loop-shaped flexible membrane. The subunits' heading angles are fixed with respect to the membrane and can only move forward and backward orthogonal to the tangent of the membrane at their connection point. However, the robot can achieve complex motions by selectively activating or deactivating the subunits using optimization techniques, further discussed in Section III. To enable particle jamming, the membrane is filled with hollow spheres.

A. Modular Subunit

Fig. 1(b) and (c) shows the subunit components including a wheg driven by a geared dc motor (Polulu 2371), two vibration motors to reduce the subunit friction with the ground (Parallex RB-Plx-314), and a miniature vacuum pump (Tulead Micro Air Pump B07W4HQX5H) to control jamming. An Internet of Things development board (Particle PHOTONH) enables wireless control and communication with the subunits. A battery shield (Sparkfun DEV-13626) connects a 1000-mAh lithium-ion battery coupled with a buck–boost converter (Sparkfun COM-15208) to the microcontroller. Two motor drivers (Sparkfun

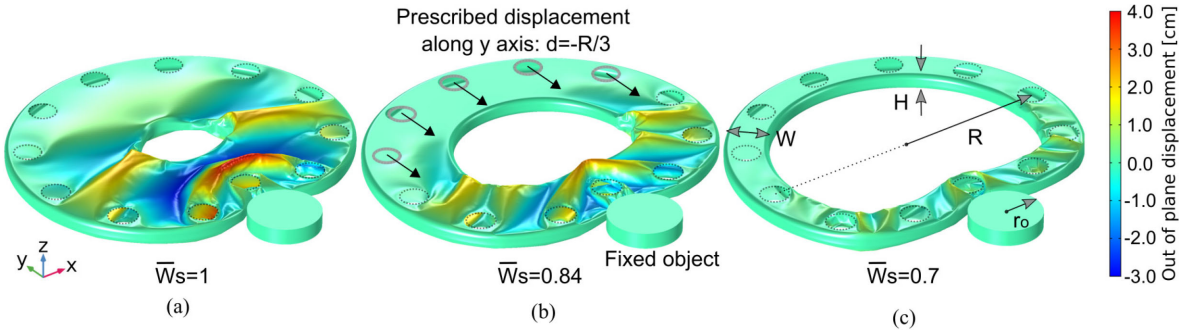

Fig. 2. Three membrane geometries modeled in COMSOL with width, W, to radius, R, ratios of (a) $W/R = 0.75$, (b) 0.5, and (c) 0.25. As shown in (b), a prescribed y displacement of $-R/3$ is applied to the five highlighted subunit mounting holes, bringing the membrane into contact with a fixed object of radius $0.2R$. The normalized stored elastic energy reduces by 30%, and the maximum out-of-plane deformation decreases from 3.9 to 1.2 cm from (a) to (c), showing the membrane's enhanced conformability.

ROB-14451) control the wheg motor, vibration motors, and vacuum pump. The whegs are covered with silicone (McMASTER-CARR 86915K22) and the subunits' mass is adjusted to 350 g using lead weights [see Fig. 1(a)] to increase the whegs' traction.

When a subunit is not responsible for locomotion, the wheg is retracted into its body and its vibration motors are activated to reduce friction between the subunit and the surface. To quantify this reduction, a load cell was connected to an individual subunit, resulting in a force of 1.6 N. The kinetic friction force of the subunit with the surface was 0.76 N with the vibration motors activated, indicating a 52% reduction compared to the wheg traction force. Alternatively, wheels would always protrude from the subunit's bottom, hindering the robot's motion when not in line with the subunit's heading. The rationale behind this design will become more evident when the control strategy is described in Section III.

The vacuum pump (minimum pressure of -44 kPa and a maximum flow rate of 2.5 L $\cdot$ s^{-1} at 5 V) air inlets are arranged in parallel such that the number of pumps alters the flow rate and, subsequently, the jamming phase transition duration, measured to be around 5 s.

B. Membrane

The membrane design was chosen to maximize conformability to facilitate object grasping, shape formation, and locomotion through narrow spaces. Low conformability of the membrane, and its associated large out-of-plane deformation [29], can harm robot performance by increasing the required driving force to conform to an object or form a desired shape, interfering with the whegs by lifting them from the surface, and increasing the robot/surface friction. Membrane conformability is influenced by many factors, including its geometry, thickness, and mechanical properties [30]. Using the membrane loop-shape design made out of polypropylene as a base design, this article focuses on the membrane width, W, to radius, R, ratio, leaving a more comprehensive optimization of the membrane properties to future studies.

Three geometries were studied using COMSOL Multiphysics 5.5's shell module, as shown in Fig. 2. The hollow membrane geometry is characterized by its width, W, radius, $R = 30$ cm, height, $H = 3$ cm, and surface thickness, $T = 100$ μm. The width-to-radius ratios of the three geometries in Fig. 2(a)–(c) varies between $W/R = 0.25$, 0.5, and 0.75, respectively. The Young's modulus $E = 1.1$ GPa, Poisson's ratio $\nu = 0.4$, and density $\rho = 0.9$ g/cm^3 match the prototype's polypropylene material. The subunit mounting holes are modeled as rigid connectors, with motion restricted along the z-axis. As shown in Fig. 2(b), a prescribed displacement of $d = -R/3$ along the y-axis is applied to the five highlighted subunit mounting holes, with no constraint on their motion along the x-axis, bringing the membrane into contact with a fixed object of radius $r_o = R/5$. We used the membrane maximum out-of-plane deformations and stored elastic energy to compare the three membranes' conformabilities and found it matches well with our experimental observations. However, other parameters may be used to quantify the conformability such as stress distributions and deformation characteristics, or time-dependent study of the membrane buckling and wrinkle formation, that could provide equal or better correlations; this is an active area of research [29]–[31].

Fig. 2(a)–(c) shows that increasing the width of the membrane from $0.25R$ to $0.75R$ increases the maximum out-of-plane deformation from about 1.2 to 3.9 cm. The deformation is driven by the elastic strain energy, W_s, stored inside the membrane during deformation [29], which reduces by 16% from case (a) to (b) and by 30% from case (a) to (c). The normalized strain energy values in Fig. 2(a)–(c) are obtained by dividing the elastic strain energy by the maximum elastic strain energy, $W_{s,\max} = 0.61$ J, corresponding to design (a). Results show that a high W/R ratio can hinder conformability and performance due to large out-of-plane deformation, a result also observed experimentally throughout the design process. The final design uses a 100-μm-thick polypropylene membrane with an 8-cm cross-sectional diameter (Aviditi Poly Tubing PT0504), which results in a width and height of approximately 10 and 2.7 cm, respectively. The larger width of the membrane compared to the subunit diameter provides room for the granular material, 1-, 2-, or 4-cm-diameter polypropylene hollow spheres (CIC Ball Company #PPH03973O, #PPH07870N, #PPH14960N), to flow along the membrane interior. The different sizes were used to experimentally characterize the robot's stiffness and

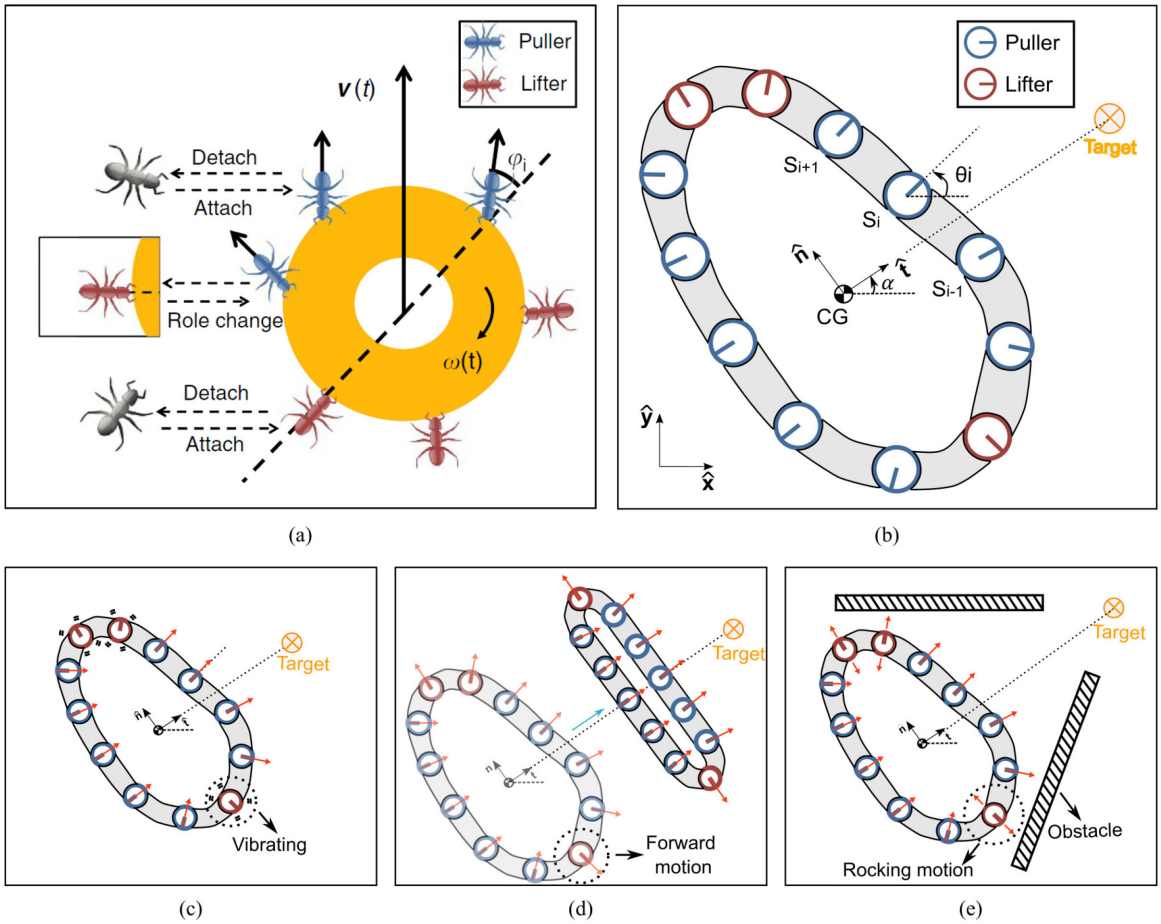

Fig. 3. (a) Ant collective transporting an object by switching between roles as "pullers" and "lifters" (image taken from [32] ©2015 https://creativecommons.org/licenses/by/4.0/CC BY 4.0). (b) Robot schematic and the position tracking parameters (top view). The circles indicate the subunits (S_i), and the radial lines show the heading angle. $\hat{\mathbf{t}}$, which points from the robot's center of geometry to the target, and $\hat{\mathbf{n}}$ define the local coordinate system, which is rotated α from the global coordinate frame. (c) In a simple target tracking task, the pullers (blue circles) provide thrust toward the target and the lifters (red circles) reduce their friction by stowing their wheg and vibrating. (d) Target tracking with alignment. The lifter subunits move orthogonal to the target, which stretches the robot, aligns more subunits toward the target, increases the number of pullers, and increases locomotion speed. (e) Target tracking through a narrow corridor. The lifters perform a 0.2-Hz rocking motion to prevent the robot from becoming stuck.

object handling properties. To install the subunits, mounting holes 30% smaller than the subunits' diameter were punched onto the membrane to create an airtight seal after installing the subunits.

C. Experimental Test Setup

The test stage was covered with paper (Savage SAV461253). Subunits' poses were visually tracked in real time [33] with an overhead webcam (Logitec Brio 960-001105). Real-time localization and control was conducted in the Robot Operating System (ROS) . A dual-range force sensor (Vernier SEN-12873) measured pulling loads.

III. Control

This section describes the control methodology for target tracking and shape formation.

A. Target Tracking

The ability to transition between soft and rigid states can be advantageous to tracking, conforming to, and moving an object. The robot can maneuver through obstacle-strewn environments and conform to objects while soft. The stiff mode can be used to firmly grasp an object, apply larger forces to move it, and locomote faster by eliminating deformation.

1) Inspiration: Since the subunits are fixed in the membrane and can only move forward and backward, not all of the subunits can provide thrust toward the target. To track the target under these constraints, we draw inspiration from recent work on ant collectives cooperatively moving an object [32], [34]. Ants work together such that they are classified either "lifters" that lift the object or "pullers" that affect which direction the object is being carried [see Fig. 3(a)]. Ants switch roles randomly and leave and rejoin the effort to carry the object at random times. A few puller ants attached to the load are able to steer the object while being supported by an army of lifter ants.

We use optimization to select the subunits that will move the robot toward the target, the "pullers." The other subunits, the "lifters," assist by reducing their friction with the surface by retracting their wheg inside the body cavity and activating their vibration motors, as explained in Section II-A.

One difference between the robot and ant collective is that ants rarely push the object (see the puller ants gathered to the object's front in Fig. 3(a) [32]). But the subunits can move both forward and backward to pull and push the robot. Thus, as shown in Fig. 3(b), the puller subunits are both on the front and back of the robot (with respect to the target).

2) Implementation: The cost function to choose the subunit's role accounts for the robot's translation only, which allows the robot body to freely rotate. Similar to ant collectives, the subunits will randomly change their roles as pullers and lifters due to the robot's nondeterministic rotation. Additionally, the cost function only accounts for each individual subunit's heading angle with respect to the robot's desired direction of motion to compute its control input. This technique results in a highly efficient linear optimization problem that enables high scalability.

To define the target tracking cost function, the subunit i's wheg's force on the surface, $\mathbf{f}_i$, is first defined as

$$\mathbf{f}_i = \eta_i f_w \left(\cos(\theta_i - \alpha)\hat{\mathbf{t}} + \sin(\theta_i - \alpha)\hat{\mathbf{n}}\right) \tag{1}$$

where $\hat{\mathbf{t}}$ and $\hat{\mathbf{n}}$ are the axes of the robot local coordinate system [see Fig. 3(b)], $\eta_i \in \{-1, 0, 1\}$ is the optimization variable to determine the direction of motion of subunit i (backward, none, or forward), $f_w = 1.6$ N is the magnitude of the wheg traction force, θ_i is subunit i's heading angle, and α is the rotation of the robot's local coordinate system [see Fig. 3(b)].

If subunit i is inactive ($\eta_i = 0$), the sliding friction $\mathbf{f}_{k,i}$ is

$$\mathbf{f}_{k,i} = (1 - |\eta_i|) f_k \hat{\mathbf{t}} \tag{2}$$

where $f_k = 0.76$ N is the kinetic friction of the subunit body with ground when vibrating. This assumes that the subunit will be pulled toward the target along the $\hat{\mathbf{t}}$-axis.

Combining the subunit sliding friction, $\mathbf{f}_{k,i}$, and the wheg's traction force, $\mathbf{f}_i$, each subunit's cost function is defined as

$$J_i = |\mathbf{f}_i \cdot \hat{\mathbf{n}}| - \mathbf{f}_i \cdot \hat{\mathbf{t}} + \mathbf{f}_{k,i} \cdot \hat{\mathbf{t}}. \tag{3}$$

The cost function minimizes the summation of the absolute value of all subunits' force along the $\hat{\mathbf{n}}$-axis. This minimizes the deviation of all subunits in both the positive and negative $\hat{\mathbf{n}}$-direction and maximizes the traction forces along $\hat{\mathbf{t}}$. Since the subunits always provide thrust in the positive $\hat{\mathbf{t}}$-direction, we can assume $\sum_{i=1}^{N} \eta_i f_w \cos\theta_i = \sum_{i=1}^{N} |\eta_i f_w \cos\theta_i|$.

The total cost function for target tracking, $J_{\text{tracking}} = \sum_{i=1}^{N} J_i$, is then given as

$$\sum_{i=1}^{N} \left(|\eta_i f_w \sin(\theta_i - \alpha)| - |\eta_i f_w \cos(\theta_i - \alpha)| + (1 - |\eta_i|) f_k\right). \tag{4}$$

Approximating $|\cos(\theta_i - \alpha)| - |\sin(\theta_i - \alpha)|$ as $\cos(\theta_i - \alpha)^2 - \sin(\theta_i - \alpha)^2$ yields

$$J_{\text{tracking}} \approx \sum_{i=1}^{N} \left(-|\eta_i| f_w \cos(2(\theta_i - \alpha)) + (1 - |\eta_i|) f_k\right) \tag{5}$$

which is a linear function of $|\eta_i|$. Finally, the optimization problem is given as

$$\min_{|\eta_i|} J_{\text{tracking}} \qquad 0 \le |\eta_i| \le 1. \tag{6}$$

Since (6) is a linear optimization problem, the result will always be on the feasible region's vertices, i.e., $|\eta_i| \in \{0, 1\}$.

If $-\frac{f_k}{f_w} \le \cos(2(\theta_i - \alpha))$, i.e., the subunit's heading angle is nearly aligned to the robot's heading angle (the $\pm\hat{\mathbf{t}}$-direction), then the derivative of the cost function with respect to $|\eta_i|$, $\frac{\partial J_{\text{tracking}}}{\partial |\eta_i|} = -f_w \cos(2(\theta_i - \alpha)) - f_k = 0$, shows that activating subunit i ($|\eta_i| = 1$) will reduce the cost function. If this condition is not met for subunit i, then deactivating the subunit (i.e., $|\eta_i| = 0$) will be the optimum solution. Note that if $|\eta_i| = 1$, the sign of η_i can be determined based on the presumed condition $0 \le \eta_i \cos(\theta_i - \alpha)$.

a) Target tracking with alignment: The lifter subunits can perform tasks other than just reducing their friction. For example, if the lifters all move forward, as shown in Fig. 3(d), they will stretch the robot to gradually align it, so more subunits face the target and the number of pullers is increased. When the robot is completely stretched into what resembles a thin ellipse, the lifters are approximately equally spread at both sides of the robot and will cancel out each other's forces. Therefore, the lifters will not prevent the robot from moving toward the target. In this case, the motion of the pullers does not change, and they continue pulling/pushing the robot toward the target. The downside of this approach is increased friction of the lifters with the ground. However, since the number of pullers is increased, there will be fewer lifters and, subsequently, a higher locomotion force for the robot as a whole.

To assess the robot's alignment, we introduce the "normalized alignment" variable, NA, which measures how well the subunits are aligned to the $\pm\hat{\mathbf{t}}$-direction as

$$NA \equiv \frac{\sum_{i=1}^{N} |\cos(\theta_i - \alpha)|}{N} \tag{7}$$

and can vary between 0 and 1. If $NA = 1$, then all the subunits are fully aligned with the $\hat{\mathbf{t}}$-axis. If $NA = 0$, then all of the subunits are orthogonal to the $\hat{\mathbf{t}}$-axis. We use this parameter as a criterion to activate jamming and preserve the robot configuration once it is sufficiently aligned toward the target. The closed-loop algorithm to combine target tracking, alignment, and jamming is shown in Algorithm 1.

b) Target tracking in a corridor: When traveling through a narrow corridor, we used another ant characteristic, an emergent oscillatory motion that helps the collective escape dead ends and bypass obstacles [34]. To implement this, the lifters implement a 0.2-Hz rocking motion [see Fig. 3(e)].

B. Shape Formation

In this section, we explain the approach to shape formation by defining a new cost function assuming that subunit i's position, $\mathbf{X}_i = [x_i, y_i]$, and heading angle are known

$$J_{\text{shape}} = \sum_{i=1}^{N} \|\mathbf{X}_{i,k} - \mathbf{X}_{i,d}\|^2 = \sum_{i=1}^{N} \|\Delta\mathbf{X}_{i,d} - \Delta\mathbf{X}_{i,k}\|^2 \tag{8}$$

where $\mathbf{X}_{i,k}$ is subunit i's position at time k, $\mathbf{X}_{i,d}$ is subunit i's desired position, and $\Delta\mathbf{X}_{i,m} = \mathbf{X}_{i,k+1} - \mathbf{X}_{i,m}$ ($m = k,\ d$). Due to the robot's relatively low speed, the subunits' heading angles update at each time step and are considered constant between

Algorithm 1: Target Tracking With Alignment and Jamming.

Given
Subunit position $\{x_1, y_1, x_2, y_2, \ldots, x_N, y_N\}$
Subunit heading $\{\theta_1, \theta_2, \ldots, \theta_N\}$ $\triangleright -\pi \leq \theta_i \leq \pi$
Target position $\{x_o, y_o\}$
Optimization variables $\{\eta_1, \eta_2, \ldots, \eta_N\}$
$\triangleright \eta_i \in \{-1, 0, 1\}$
Jamming included $\in$ { True, False }
while $\bigcap_{i=1}^{N} \|(x_i - x_o)^2 + (y_i - y_o)^2\| > 15$ cm **do**
  Compute NA from (7)
  if $NA < NA_{\text{desired}}$ **then**
    Compute η_is for target tracking with alignment
  else if $NA_{\text{desired}} \leq NA$
    ifJamming included**then**
      Activate jamming
    end if
    Compute η_is for target tracking without alignment
  end if
  for $i = 0$ to N**do**
    if $\eta_i = 1$ **then**
      Subunit i moves forward
    if $\eta_i = -1$**then**
      Subunit i moves backward
    if $\eta_i = 0$**then**
      Subunit i stows-in its wheg and vibrates
    end if
  end for
end while

k and $k+1$. Under this assumption, subunit i's displacement from k to $k+1$ can be simplified as

$$\Delta \mathbf{X}_{i,k} = \eta_{i,k} \left\| \bar{\mathbf{V}}_{i,k} \right\| \delta t (\cos(\theta_{i,k}) \hat{\mathbf{x}} + \sin(\theta_{i,k}) \hat{\mathbf{y}}) \quad (9)$$

where $\hat{\mathbf{x}}$ and $\hat{\mathbf{y}}$ are the global reference frame unit vectors, and $\bar{\mathbf{V}}_{i,k}$ is the subunit's average velocity [see Fig. 4(a)]. Equations (8) and (9) can be combined (dropping subscript k for clarity) into

$$J_{\text{shape}} = \sum_{i=1}^{N} \Big[\left(\eta_i \left\| \bar{\mathbf{V}}_i \right\| \delta t\right)^2 + \|\Delta \mathbf{X}_{i,d}\|^2 - 2\eta_i \left\| \bar{\mathbf{V}}_i \right\| \delta t \, \|\Delta \mathbf{X}_{i,d}\| \cos(\angle \Delta \mathbf{X}_{i,d} - \theta_i) \Big]. \quad (10)$$

The minimization problem is then $\min_{\eta_i} J_{\text{shape}}$ subject to $\eta_i \in \{-1, 0, 1\}$.

The optimization problem is solved in two ways. If either $\cos(\angle \Delta \mathbf{X}_{i,d} - \theta_i)$ or $||\Delta \mathbf{X}_{i,d}||$ is zero, by substituting into (10), the optimum solution will be $\eta_i = 0$. Otherwise, the difference of the cost function for the two cases, $J_{\text{shape},\ \eta_i \neq 0} - J_{\text{shape},\ \eta_i = 0}$, is calculated as

$$\left\| \bar{\mathbf{V}}_i \right\| \delta t \left(\left\| \bar{\mathbf{V}}_i \right\| \delta t - 2\eta_i \|\Delta \mathbf{X}_{i,d}\| \cos(\angle \Delta \mathbf{X}_{i,d} - \theta_i) \right). \quad (11)$$

According to (11), if $||\Delta \mathbf{X}_{i,d} \cos(\angle \Delta \mathbf{X}_{i,d} - \theta_i)|| > \|\bar{\mathbf{V}}_i\| \delta t / 2$, the optimum solution is $\eta_i = \text{sign}(\cos(\angle \Delta \mathbf{X}_{i,d} - \theta_i))$; otherwise, it is $\eta_i = 0$. We do not have the solution to the full dynamics of the robot, which would compute $\|\bar{\mathbf{V}}_i\| \delta t$ for each subunit; thus, we upper bound it as $\|\bar{\mathbf{V}}_i\|_{\max} \delta t = 4$ cm using the dc motor specs (60-r/min no-load speed at 5 V), wheg periphery (4 cm), and assuming a time step of $\delta t = 1$ s.

In summary, if $||\Delta \mathbf{X}_{i,d} \cos(\angle \Delta \mathbf{X}_{i,d} - \theta_i)|| > 2$ cm, then $\eta_i = \text{sign}(\cos(\angle \Delta \mathbf{X}_{i,d} - \theta_i))$; otherwise, $\eta_i = 0$. Fig. 4 illustrates the subunits' motion for various shapes, which are also demonstrated experimentally in Section V-C.

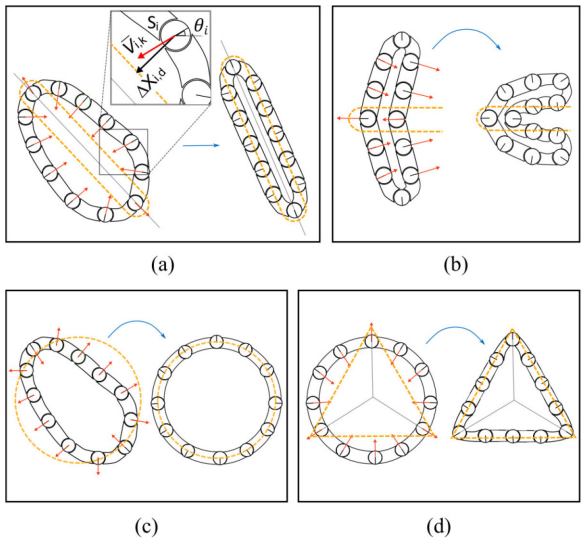

Fig. 4. Subunit motions when forming (a) line, (b) C-shape, (c) circle, and (d) triangle.

IV. Simulation

We used the ProjectChrono simulation engine with the Euler implicit linearized time stepper, the projected symmetric successive over-relaxation solver, and the Chrono::SolidWorks add-on to study locomotion and control [35]. Subunits are modeled by contact body 1 in Fig. 5. The contact body's diameter is larger than the subunit diameter to adjust the maximum bending angle among subunits to match the prototype, $\approx 90^\circ$. Three spherical contact bodies create the robot's contact points with the ground (contact bodies 2–4). The wheg's contact body is modeled as a set of six evenly distributed cylinders (contact bodies 5–10). The membrane was modeled as two rigid links between two subunits with two rotational DOFs, as shown by Links 1 and 2 in Fig. 5.

To verify the simulation, we compared it to an experimental target tracking with alignment task [see Movie S1 in the supplementary material and Fig. 6(a)]. The simulation path is more uniform due to a lack of external disturbances and fewer DOFs in the membrane. Fig. 6(b) shows the distance to the target versus time and demonstrates a similar trend. The simulation's mean velocity is within 13% of the experiment's, sufficiently close for qualitative comparisons. Fig. 6(c) compares the normalized alignments [see (7)]. We use the simulation in the next section to study the robot behavior as the number of subunits is increased.

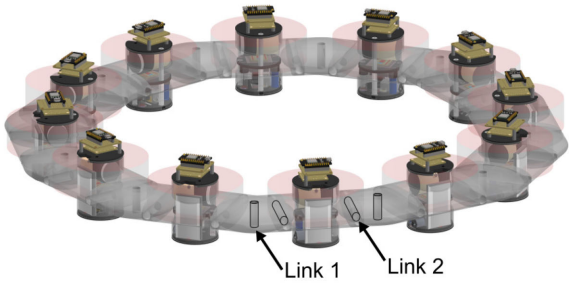

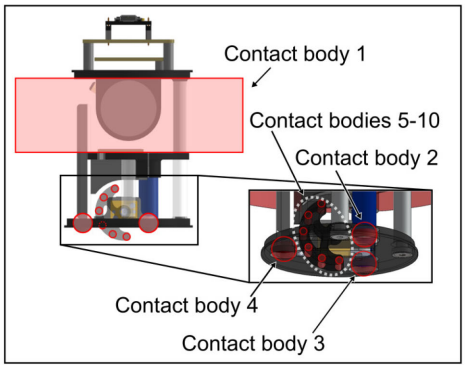

Fig. 5. Simulation model. The simple contact body definitions are highlighted in red, and the two rotational DOF among the rigid links are depicted by Links 1 and 2.

V. Results and Discussions

This section covers the experiment and simulation results, including stiffness characterization, object handling, locomotion, corridor navigation, and robustness to subunit failure.

A. Mechanical Characterization

The robot's stiffness can be modulated to improve performance, most importantly in locomotion and moving an object after grasping. In general, the robot should be highly conformable in its soft state and as stiff as possible when jammed. In addition to the effect of the membrane geometry, which was discussed in Section II-B, vacuum pressure and granular material properties such as particle size, shape, friction, and volume fraction affect conformability and jamming stiffness.

To study the effect of the particle size and volume fraction, the ratio of the particle volume to the interior volume of the membrane in its fully inflated state, we measured the robot's stiffness in the soft and jammed states using a compression test platform [see Fig. 7(a)]. In each test, the vacuum pressure was changed between 0 kPa (soft state) and 44 kPa (jammed state), and the interior particle size and volume fraction were changed by using hollow polypropylene spheres with three diameters, i.e., 1, 2, and 4 cm, resulting in membrane width-to-particle diameter ratios of $W/d = 10$, 5, and 2.5, respectively.

The robot was placed between the compressing plates in a C-shape configuration [see Fig. 7(a)] to provide insight on the robot's object handling capabilities and its ability to preserve its configuration. The volume fraction was varied for each particle size between 20%, 30%, and 40%.

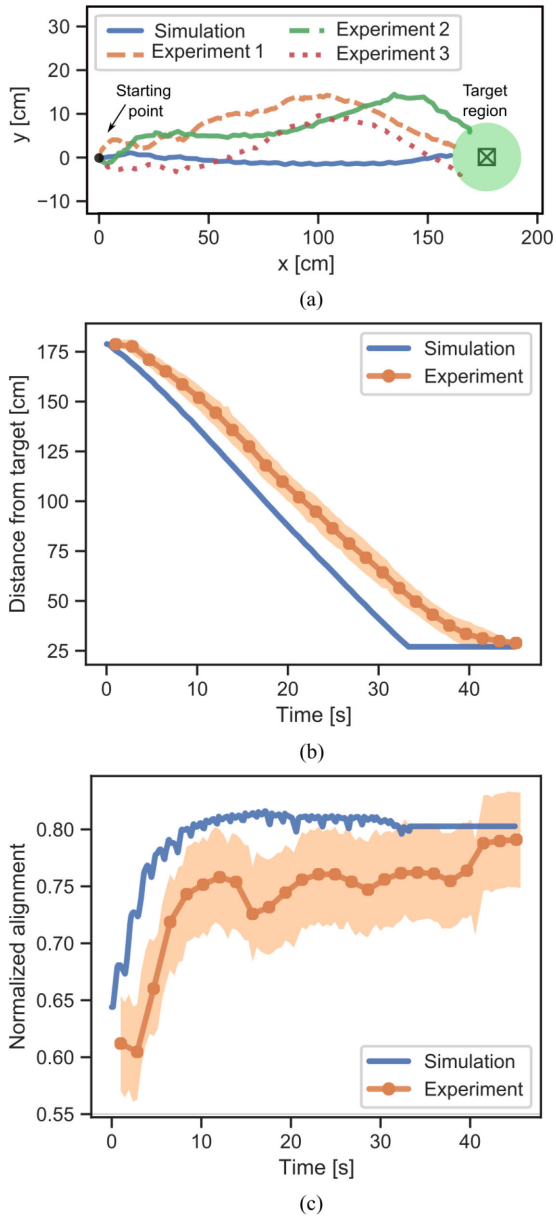

Fig. 6. (a) Experimental and simulated paths in a target tracking with alignment task. (b) Distance from the robot's center to the target. (c) Normalized alignment. The desired normalized alignment was chosen by trial and error to achieve a smooth performance (0.8 simulation and 0.75 experiments) and experimental results are averaged over five trials.

Fig. 7(b) and (c) shows the results for 1-cm particles with a 40% volume fraction in the jammed and unjammed states. The results show a nonlinear strain-stiffening behavior. In Fig. 7(b), depending on exactly how the compressing plates engaged the robot, the first few centimeters of displacement typically produced only little force even in the jammed state, while in the initially unjammed state [see Fig. 7(c)], a sufficiently large displacement led to mild jamming. Therefore, the robot's average stiffness plotted in Fig. 7(a) is calculated as the average of the slope of the force–displacement curve over the full displacement range shown, computed at 2-cm intervals.

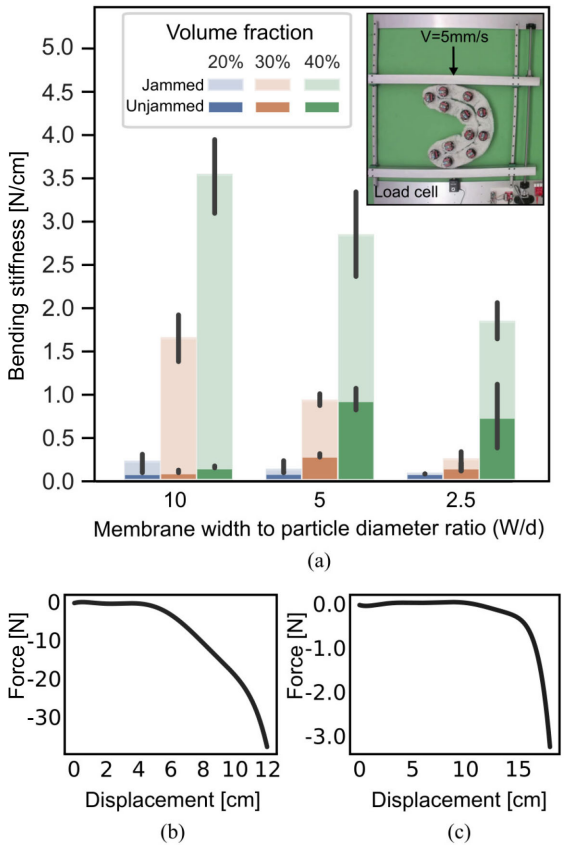

Fig. 7. Compression stiffness test averaged over five trials; error bars show standard deviation. The membrane width, W, is 10 cm and the particle are $d = 1$ cm, 2 cm, and 4 cm. Force–displacement curves are shown for 1-cm particles and 40% volume fraction in (b) jammed and (c) unjammed states.

Fig. 7(a) shows that a smaller particle size leads to both higher jammed stiffness and significantly lower unjammed stiffness, especially for the maximum volume fraction (40%). In addition, increasing the volume fraction increased both the jammed and unjammed stiffness for all particle sizes. For instance, with 1-cm particles, the jammed stiffness increases approximately 600% when increasing the volume fraction from 20% to 30%, and the stiffness roughly doubled again when raising the volume fraction from 30% to 40%.

The jammed stiffness increases with a higher volume fraction due to the higher number of particles, which leads to more contact points. This results in more work required to overcome friction and deform the robot in the jammed state.

The increase in unjammed stiffness seen in Fig. 7(c) beyond 15-cm results because the robot's deformation is so large that the available internal volume of the now buckled and wrinkled membrane falls below the jamming threshold and produces a passively jammed state [36]. For the 2- and 4-cm particles, the membrane-diameter-to-particle-diameter ratio (W/d) is sufficiently small that finite size effects become important. This means that the interaction between the particles and the membrane will become much more significant, especially once the membrane buckles in compression. As a result, there is a significant jump in the unjammed stiffness for the 2- and 4-cm particle samples at 40% volume fraction.

For the prototype, we, therefore, used 1-cm particles with a 40% volume fraction, given its high stiffness when jammed and high compliance when not jammed.

B. Object Handling

The robot's high conformability and tunable stiffness enable it to approach an object, conform to it, secure the grasp by jamming, and pull or push the object (see Movie S2 and Movie S3 in the supplementary material). To test the effect of volume fraction and particle size, we performed a pulling test [see Fig. 8(a)–(c)] on a 0.5-kg 5-cm-diameter cylinder and a 0.5-kg 5-cm-wide cube. Both were covered with paper to maintain consistent surface friction. For each particle size, the maximum pulling force for three volume fractions [20%, 30%, and 40%; see Fig. 8(d) and (e)] was tested. The results show the same trend for both objects, but the maximum pulling force for the cube is always greater, probably because the cube's sharp edges resulted in a better grip.

According to the experiments, the best volume fractions for 1-, 2-, and 4-cm particles are 40%, 30%, and 20%, respectively. This trend shows that increasing the size of the granular particles decreases the optimum volume fraction. This is explained by the results in Fig. 7(a), which shows that the robot's conformability decreases when reducing the W/d ratio and increases when reducing the particle volume fraction.

More importantly, the experimental results show that the maximum grasping force belongs to the smallest particle size. Fig. 7(a) shows that the 1-cm particle size has both the highest conformability and the highest jammed stiffness, which both positively affect the maximum grasping force. For 1-cm particles with 40% volume fraction, the robot's maximum pulling force, $\approx$17 N, is reached while jammed for both the cube and the cylinder [see Fig. 8(d) and (e)] because the objects were not released and the pulling force was limited to the robot traction force.

Fig. 8 shows the pulling force difference between jammed and unjammed states. The difference is not proportional to the stiffness variation results in Fig. 7. To explain this, note that parameters other than stiffness, such as the subunits' locomotion force and the robot/object contact physics, may also affect the maximum pulling force. In addition, as shown in Fig. 7, the system has a nonlinear force–displacement profile that indicates that stiffness depends on the initial jammed configuration and its loading mode. Therefore, although the compression test is used as a reference for qualitative analysis, the actual stiffness variation may be scenario dependent.

C. Shape Formation

Shape formation enables the robot to optimize its configuration for various tasks (see Fig. 9 and Movie S4 in the supplementary material). For instance, forming a C-shape is useful for grasping an object as shown in Section V-B, a triangular shape is useful for pushing an object as shown in Movie S5

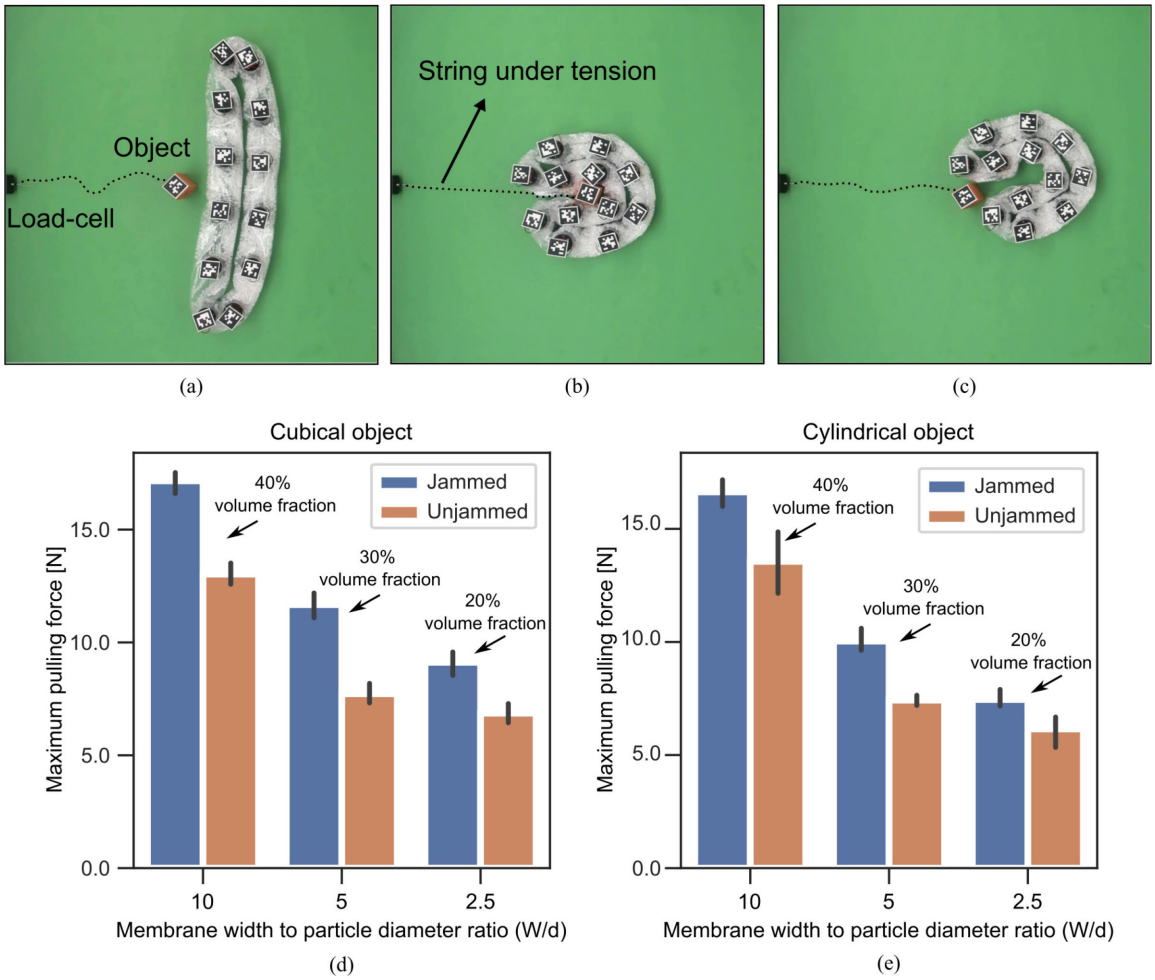

Fig. 8. Robot (a) engulfing an object connected to a load cell, (b) pulling it away from the load cell in jammed mode, and (c) releasing the object. (d) and (e) show the maximum pulling force averaged over five tests for a cube and a cylindrical object, respectively. Error bars show the standard deviation. Three particle sizes and three volume fractions of each particle size were tested on each object. The maximum pulling force of each particle size and their corresponding volume fractions are displayed for both objects. The highest pulling forces for 1-, 2-, and 4-cm particle sizes ($W/d = 10$, 5, and 2.5) are achieved with 40%, 30%, and 20% volume fraction, respectively. For 1-cm particles at 40% volume fraction, the maximum pulling force is reached while jammed since the object was not released and the pulling force was limited to the traction force.

in the supplementary material, and a line shape can be used to maximize the locomotion force or pass through a narrow corridor, as described in Section V-E.

D. Target Tracking

In this section, we demonstrate three different cases of target tracking. The first tracks a target position without alignment or jamming. The second uses the alignment algorithm and the third adds jamming. Movie S6 in the supplementary material shows all three cases.

Fig 10(a) shows that when the target tracking with alignment method is used, the robot's mean velocity significantly increases as the subunit heading angles align toward the target. Moreover, the results demonstrate an additional 20% improvement in the average velocity when jamming is activated due to eliminating the robot's deformation during locomotion.

The robot's normalized alignment is shown in Fig. 10(b) for the three target tracking cases. The results show that the normalized alignment randomly oscillates in the case of target tracking without alignment, whereas it converges to its desired value, 0.75, in the case of target tracking with alignment and target tracking with alignment and jamming. In addition, the normalized alignment has less oscillation once it reaches its desired value in the case of target tracking with jamming, which shows the capability of the jamming feature to preserve a desired configuration of the robot during locomotion.

To study target tracking when the number of subunits is scaled up, we relied on the simulation environment. The robot was given the same target tracking with alignment task for all cases (see Movie S7 in the supplementary material). Fig. 11 shows that the locomotion speed asymptotically decreases when increasing the number of subunits (up to 35% when the subunits are scaled up $8\times$). By increasing the number of subunits, the robot undergoes more deformation, which subsequently decreases the robot's

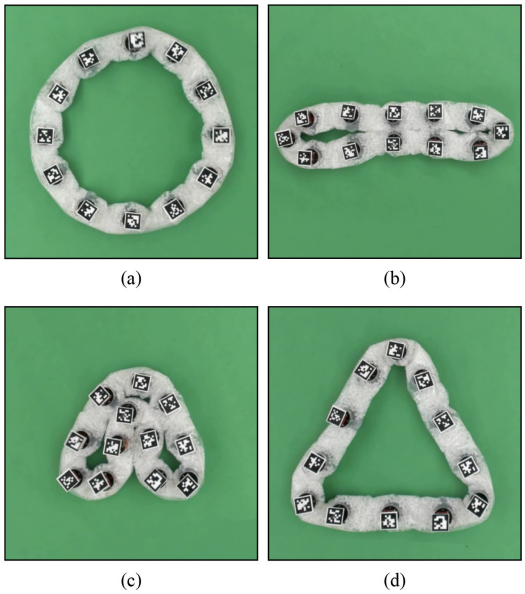

Fig. 9. Robot performing shape formation for a (a) circle, (b) line shape, (c) C-shape, and (d) triangle.

speed. To reduce this effect when scaling up the number of subunits, jamming can be employed to increase the robot's speed.

E. Narrow Corridor Passing

Fig. 12 shows the robot passing through a narrow corridor with two initial configurations while applying the 0.2-Hz rocking motion to the "lifters," as described in Section III-A.

F. Robustness to Failure

The robot's distributed design preserves functionality if some subunits fail. Fig. 13 shows the outcome when zero, two, four, and six subunits fail (mimicked here with a disconnected battery) in a target tracking task. The robot was initialized in a jammed circular shape. The results show that the robot's mean velocity decreases with the same trend as the robot's normalized driving force in the direction toward the target, estimated as

$$\bar{f}_{\text{active}} \equiv \frac{\sum_{i\in\text{Active subunits}} |\cos(\theta_i - \alpha)|}{\sum_{i=1}^{N} |\cos(\theta_i - \alpha)|}. \tag{12}$$

Note that $\bar{f}_{\text{active}}$ is normalized with respect to the maximum driving force of the robot in a circular configuration, i.e., $\bar{f}_{\text{active}} = 1$ when all subunits are active, and $\bar{f}_{\text{active}} = 0$ when all subunits fail. Additionally, $\bar{f}_{\text{active}}$ is the same for the case of two and four failed subunits, since the additional two failed subunits in the latter case are initially perpendicular to the robot's direction of motion ($\cos(\theta_i - \alpha)$ is zero for these subunits). However, the experimental result shows a slightly lower average velocity for the case of four failed subunits, which we believe is due to random rotation of the robot, which changes the heading of the failed subunits, changing their role from lifter to pullers, in addition to the inactive vibration motors of the failed subunits,

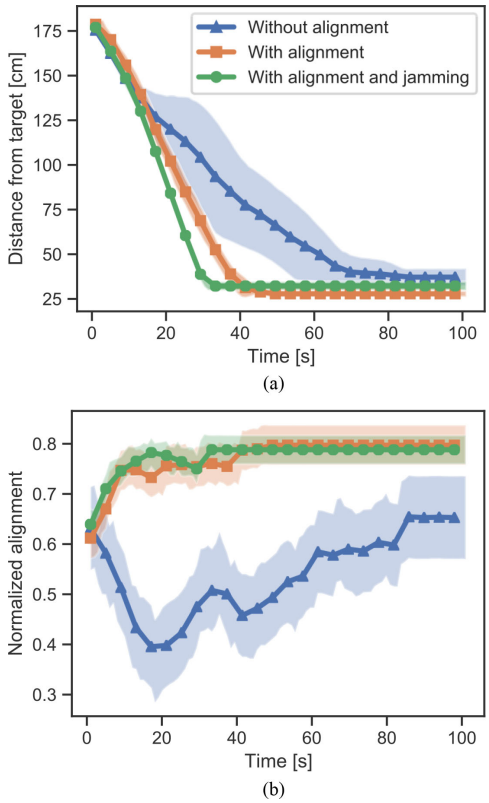

Fig. 10. (a) Distance to target (measured from the robot's center, about ≈25 cm when the periphery reaches the target) and (b) normalized alignment versus time in target tracking without alignment, with alignment, and with alignment and jamming. Results are averaged over five trials.

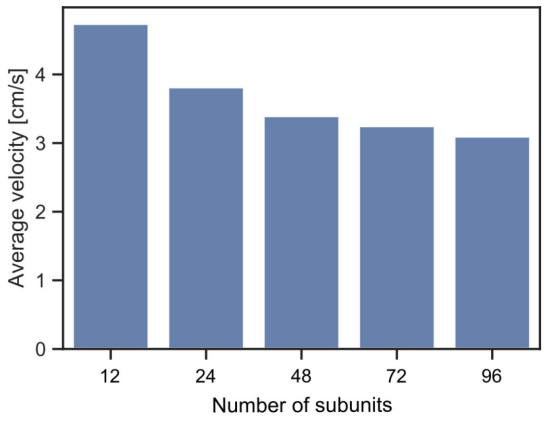

Fig. 11. Simulation results of robot average velocity versus number of subunits in a target tracking with alignment task.

which leads to higher sliding friction. In the most extreme case, with six subunits failed, the average velocity is reduced by 40%.

VI. Conclusion

In this article, the prototype design, fabrication, and optimization-based control methodologies to track a target and perform shape formation of a new type of soft robot based on boundary-constrained modular subunits were described. The design introduces both softness and modularity by using rigid robotic subunits that are flexibly connected to each other by a

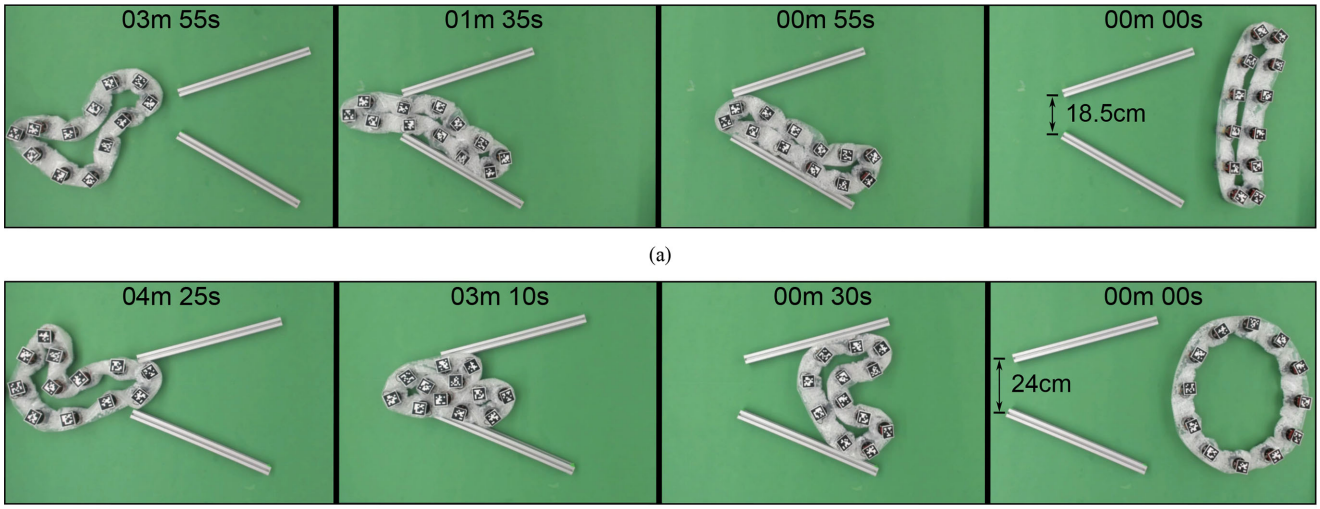

Fig. 12. Robot passing through a narrow corridor in a (a) line-shape and (b) circular initial configuration (see Movie S8 in the supplementary material).

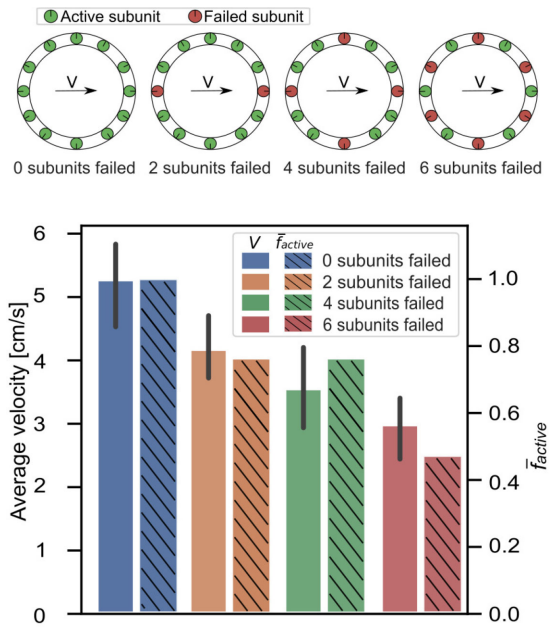

Fig. 13. (Top) subunit failure cases and (bottom) the mean robot velocity averaged over three trials; error bars show standard deviation. $\bar{f}_{\text{active}}$ from (12) is the sum of the active subunits' driving force in the direction of the target normalized with respect to the robot's maximum driving force in a circular configuration. The robot's velocity decreases with a similar trend to $\bar{f}_{\text{active}}$ as the number of failed subunits increases.

soft toroidal membrane. The robot is able to perform both as a soft and rigid system by using a granular jamming mechanism activated by a distributed on-board vacuum system.

The granular jamming mechanism and the object handling capability were characterized as a function of particle size and volume fraction. The results showed that the smallest particle size exhibited both the highest conformability and jammed stiffness. The result was verified by object grasping and pulling tests. The robot exhibits capabilities of traditional elastomeric soft robots, such as squeezing through a narrow corridor and safe and robust object handling. In addition, the robot demonstrates many advantages of using a modular design for soft robots, including decentralized locomotion, robustness to partial failure of its components, and a tetherless design.

The robot can form different shapes to enhance locomotion and object handling. Jamming can further improve performance by preserving a desired configuration during locomotion or increasing the pulling force during object grasping.

A multibody dynamic simulation compared the robot's performance in a target tracking task as the number of subunits was scaled up. The results showed that the robot's average velocity decreases asymptotically as the number of subunits is increased. Our understanding is that the higher scale design resembles a softer system that deforms more and, therefore, leads to more energy dissipation during locomotion.

In future studies, we plan to implement distributed local sensing and control to the system so that the robot does not need to rely on an external tracking system for pose feedback.

ACKNOWLEDGMENT

The authors would like to thank Ryan Higashi for his help designing and fabricating the compression test setup and the robot as well as Bruno-Pier Busque for his work on the tracking system.

REFERENCES

[1] J.-H. Lee, Y. S. Chung, and H. Rodrigue, "Long shape memory alloy tendon-based soft robotic actuators and implementation as a soft gripper," *Sci. Rep.*, vol. 9, no. 1, 2019, Art. no. 11251.

[2] J. R. Amend, E. Brown, N. Rodenberg, H. M. Jaeger, and H. Lipson, "A positive pressure universal gripper based on the jamming of granular material," *IEEE Trans Robot.*, vol. 28, no. 2, pp. 341–350, Apr. 2012.

[3] V. Alizadehyazdi, M. Bonthron, and M. Spenko, "An electrostatic/gecko-inspired adhesives soft robotic gripper," *IEEE Robot. Autom. Lett.*, vol. 5, no. 3, pp. 4679–4686, Jul. 2020.

[4] M. C. Carrozza *et al.*, "A cosmetic prosthetic hand with tendon driven under-actuated mechanism and compliant joints: ongoing research and preliminary results," in *Proc. IEEE Int. Conf. Robot. Autom.*, 2005, pp. 2661–2666.

[5] R. K. Katzschmann, J. DelPreto, R. MacCurdy, and D. Rus, "Exploration of underwater life with an acoustically controlled soft robotic fish," *Sci. Robot.*, vol. 3, no. 16, 2018, Art. no. eaar3449.

[6] H. M. Jaeger, "Celebrating soft matter's 10th anniversary: Toward jamming by design," *Soft Matter*, vol. 11, no. 1, pp. 12–27, 2015.

[7] M. Brancadoro, M. Manti, S. Tognarelli, and M. Cianchetti, "Fiber jamming transition as a stiffening mechanism for soft robotics," *Soft Robot.*, vol. 7, no. 6, pp. 663–674, 2020.

[8] Y. Narang, B. Aktaş, S. Ornellas, J. Vlassak, and R. Howe, "Lightweight highly tunable jamming-based composites," *Soft Robot.*, vol. 7, no. 6, pp. 724–735, 2020.

[9] E. Steltz, A. Mozeika, J. Rembisz, N. Corson, and H. M. Jaeger, "Jamming as an enabling technology for soft robotics," *Proc. SPIE*, vol. 7642, 2010, Art. no. 764225.

[10] Y. Yang, Y. Zhang, Z. Kan, J. Zeng, and M. Y. Wang, "Hybrid jamming for bioinspired soft robotic fingers," *Soft Robot.*, vol. 7, no. 3, pp. 292–308, 2019.

[11] S. Hauser, M. Robertson, A. Ijspeert, and J. Paik, "JammJoint: A variable stiffness device based on granular jamming for wearable joint support," *IEEE Robot. Autom. Lett.*, vol. 2, no. 2, pp. 849–855, Apr. 2017.

[12] D. Rus and M. T. Tolley, "Design, fabrication and control of soft robots," *Nature*, vol. 521, no. 7553, pp. 467–475, 2015.

[13] F. Schmitt, O. Piccin, L. Barbé, and B. Bayle, "Soft robots manufacturing: A review," *Front. Robot. AI*, vol. 5, 2018, Art. no. 84.

[14] M. E. Sayed, J. O. Roberts, R. M. McKenzie, S. Aracri, A. Buchoux, and A. A. Stokes, "Limpet II: A modular, untethered soft robot," *Soft Robot.*, vol. 8, no. 3, pp. 319–339, 2020.

[15] M. Yim *et al.*, "Modular self-reconfigurable robot systems [grand challenges of robotics]," *IEEE Robot. Autom. Mag.*, vol. 14, no. 1, pp. 43–52, Mar. 2007.

[16] A. Brunete, A. Ranganath, S. Segovia, J. P. de Frutos, M. Hernando, and E. Gambao, "Current trends in reconfigurable modular robots design," *Int. J. Adv. Robot. Syst.*, vol. 14, no. 3, 2017, Art. no. 1729881417710457.

[17] Z. Chen, C. Zhao, Y. Zhang, Y. Zhu, J. Fan, and J. Zhao, "C-Balls: A modular soft robot connected and driven via magnet forced," *J. Phys.: Conf. Ser.*, vol. 1207, no. 1, 2019, Art. no. 012006.

[18] M. P. Nemitz, P. Mihaylov, T. W. Barraclough, D. Ross, and A. A. Stokes, "Using voice coils to actuate modular soft robots: Wormbot, an example," *Soft Robot.*, vol. 3, no. 4, pp. 198–204, 2016.

[19] E. H. Østergaard, K. Kassow, R. Beck, and H. H. Lund, "Design of the ATRON lattice-based self-reconfigurable robot," *Auton. Robots*, vol. 21, no. 2, pp. 165–183, 2006.

[20] F. Mondada *et al.*, "Swarm-Bot: A new distributed robotic concept," *Auton. Robots*, vol. 17, nos. 2/3, pp. 193–221, 2004.

[21] S.-C. Chen, K.-J. Huang, W.-H. Chen, S.-Y. Shen, C.-H. Li, and P.-C. Lin, "Quattroped: A leg-wheel transformable robot," *IEEE/ASME Trans. Mechatronics*, vol. 19, no. 2, pp. 730–742, Apr. 2014.

[22] M. A. Karimi, V. Alizadehyazdi, B.-P. Busque, H. M. Jaeger, and M. Spenko, "A boundary-constrained swarm robot with granular jamming," in *Proc. 3rd IEEE Int. Conf. Soft Robot.*, 2020, pp. 291–296.

[23] K. Tanaka *et al.*, "Cable-driven jamming of a boundary constrained soft robot," in *Proc. 3rd IEEE Int. Conf. Soft Robot.*, 2020, pp. 852–857.

[24] M. Wehner *et al.*, "An integrated design and fabrication strategy for entirely soft, autonomous robots," *Nature*, vol. 536, no. 7617, pp. 451–455, 2016.

[25] S. I. Rich, R. J. Wood, and C. Majidi, "Untethered soft robotics," *Nat. Electron.*, vol. 1, no. 2, pp. 102–112, 2018.

[26] J. M. Jani, M. Leary, A. Subic, and M. A. Gibson, "A review of shape memory alloy research, applications and opportunities," *Mater. Des. (1980–2015)*, vol. 56, pp. 1078–1113, 2014.

[27] U. Gupta, L. Qin, Y. Wang, H. Godaba, and J. Zhu, "Soft robots based on dielectric elastomer actuators: A review," *Smart Mater. Struct.*, vol. 28, no. 10, 2019, Art no. 103002.

[28] A. D. Marchese and D. Rus, "Design, kinematics, and control of a soft spatial fluidic elastomer manipulator," *Int. J. Robot. Res.*, vol. 35, no. 7, pp. 840–869, 2016.

[29] H. Zhang, Z. Zhou, A. Chudnovsky, and H. Pham, "Time-dependent buckling delamination of thin plastic films and their conformability: Observations and modeling," *Int. J. Eng. Sci.*, vol. 150, 2020, Art no. 103258.

[30] W. Dong *et al.*, "Theoretical and experimental study of 2-D conformability of stretchable electronics laminated onto skin," *Sci. China Technol. Sci.*, vol. 60, no. 9, pp. 1415–1422, 2017.

[31] A. O. Sageman-Furnas, P. Goswami, G. Menon, and S. J. Russell, "The sphereprint: An approach to quantifying the conformability of flexible materials," *Textile Res. J.*, vol. 84, no. 8, pp. 793–807, 2014.

[32] A. Gelblum, I. Pinkoviezky, E. Fonio, A. Ghosh, N. Gov, and O. Feinerman, "Ant groups optimally amplify the effect of transiently informed individuals," *Nat. Commun.*, vol. 6, no. 1, 2015, Art. no. 7729.

[33] J. Wang and E. Olson, "AprilTag 2: Efficient and robust fiducial detection," in *Proc. IEEE/RSJ Int. Conf. Intell. Robots Syst.*, 2016, pp. 4193–4198.

[34] A. Gelblum, I. Pinkoviezky, E. Fonio, N. S. Gov, and O. Feinerman, "Emergent oscillations assist obstacle negotiation during ant cooperative transport," *Proc. Nat. Acad. Sci.*, vol. 113, no. 51, pp. 14 615–14620, 2016.

[35] A. Tasora *et al.*, "Chrono: An open source multi-physics dynamics engine," in *High Performance Computing in Science and Engineering*. New York, NY, USA: Springer, 2015, pp. 19–49.

[36] Y. Li, Y. Chen, Y. Yang, and Y. Wei, "Passive particle jamming and its stiffening of soft robotic grippers," *IEEE Trans Robot.*, vol. 33, no. 2, pp. 446–455, Apr. 2017.

Mohammad Amin Karimi received the B.S. degree in mechanical engineering from Semnan University, Semnan, Iran, in 2016, and the M.E. degree in mechanical and aerospace engineering in 2020 from the Illinois Institute of Technology, Chicago, IL, USA, where he is currently working toward the Ph.D. degree in mechanical and aerospace engineering.

His research interests include soft and distributed robotics.

Vahid Alizadehyazdi received the Ph.D. degree in mechanical and aerospace engineering from the Illinois Institute of Technology, Chicago, IL, USA, in 2019.

He is currently a Postdoctoral Researcher with the University of Chicago, Chicago. His research interests include robotics, sensors, and actuators.

Heinrich M. Jaeger received the Ph.D. degree in physics from the University of Minnesota, Minneapolis, MN, USA, in 1987.

He is currently the Sewell Avery Distinguished Service Professor of Physics with the University of Chicago, Chicago, IL, USA. He has been the Faculty with the University of Chicago since 1991, directing the Chicago Materials Research Center from 2001 to 2006 and the James Franck Institute from 2007 to 2010. His current research interests include self-assembled nanoparticle structures, rheology of concentrated particle suspensions, and granular material packing and flow.

Dr. Jaeger is a Fellow of the American Physical Society and an elected member of the American Academy of Arts and Sciences.

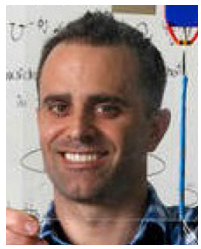

Matthew Spenko (Senior Member, IEEE) received the B.S. degree from Northwestern University, Evanston, IL, USA, in 1999, and the M.S. and Ph.D. degrees from the Massachusetts Institute of Technology, Cambridge, MA, USA, in 2001 and 2005, respectively, all in mechanical engineering.

He is currently a Professor of Mechanical Engineering with the Illinois Institute of Technology, Chicago, IL. From 2005 to 2007, he was an Intelligence Community Postdoctoral Scholar with the Center for Design Research, Stanford University, Stanford, CA, USA. His research interests include robotic mobility in challenging environments and localization safety.

Dr. Spenko is an Associate Editor for *Field Robotics*.